Journal of Materials Science and Engineering with Advanced Technology
Volume 9, Number 2, 2014, Pages 69-107

THERMAL ISSUES IN DEVELOPMENT OF AN APPARATUS TO ENABLE CHARACTERIZATION OF COATINGS

(This paper was presented at the AIAA SDM Conference, Orlando, FL April 12-15, 2010, paper# 2010-3126.)

OLIVER EASTERDAY[1], ANTHONY PALAZOTTO[1], RICHARD BRANAM[1], WILLIAM BAKER[1] and TOMMY GEORGE[2]

[1]Air Force Institute of Technology
Wright-Patterson Air Force Base
Ohio, 45433
USA
e-mail: anthony.palazotto@afit.edu

[2]Air Force Research Laboratory
Wright-Patterson Air Force Base
Ohio, 45433
USA

Abstract

Coatings have been assessed for their complex modulus in a non-contact excitation, suspension, and semi-numerical extrapolated strain field technique using a free-free beam suspended in a vacuum. Mechanical characterization of the non-linear thermal barrier coatings beyond room temperature is desirable to expand their design-space from hot- to cold-sections of turbo machinery using the TBC process techniques for HCF suppression. Modern high bypass turbo-machinery achieves around service temperatures up to about 500degC (40:1 pressure ratio) in the "cold sections". The adoption of a free-free rig to elevated temperature testing while preserving its advantageous features is highly desirable in order to characterize the coatings across the range of service temperatures. This involved some lengthy thermal validation as maintenance of

Keywords and phrases: finite element, thermal barriers coatings, heat transfer.
Received April 30, 2014

a near-isothermal specimen was critical. Thermal validation was critical as the non-contacting semi-numerical extrapolation of the strain field is from an assumed free-free mode shape; titanium undergoes about a 25% reduction in modulus variation when heated from 20 to 565degC, the design maximum. These elementary thermal issues were thought to be well-covered in the literature, but surprisingly there is little on handling of finite difference radiation boundary conditions, the Stark number lumped capacitance model, and associated FEA modelling.

Nomenclature

E = Young's (elastic) modulus (GPa).

Q = system quality factor (reciprocal of the loss-factor of the system).

η_{sys} = loss factor of the system, measured from decay.

η_{bare} = loss factor of the bare beam, measured from decay.

η_{mat} = loss factor of the TBC material.

SER = strain energy ratio. The volumetric strain energy stored in the coating over that of the beam regions.

Sk = Stark number (also known as radiation Stefan number).

L_c = characteristic length.

Bi = Biot number.

h = convective (or radiative) surface coefficient.

q = heat flow (W).

q'' = heat flux $(\mathrm{W/m^2})$.

A = surface area of solid $(\mathrm{m^2})$.

V = volume of solid $(\mathrm{m^3})$.

k = thermal conductivity $(\mathrm{W/m \cdot C})$.

l = length (m).

w = width (m).

t = thickness (m).

σ = Stefan-Boltzmann constant $(5.67 \times 10^{-8} \mathrm{W/m^2 \cdot deg\ K^4})$, or, mechanical/ thermal stress.

Δx = characteristic length (m).

h = surface convective coefficient $(\mathrm{W/m^2 \cdot C})$.

ε = surface emissivity, or, mechanical/thermal strain.

τ = optical transmissivity.

α = optical reflectivity.

E = power of emission (W).

T = temperature, absolute (K).

ω_n = resonance frequency (rad/sec or Hz).

I = irradiation flux intensity $(\mathrm{W/m^2})$.

Q, R = beam tip end fluxes, non-dimensional.

λ = non-dimensional irradiation term.

α = non-dimension aspect ratio of surface area to cross-sectional area, or, radiation absorption coefficient.

δ = non-dimension ambient temperature.

υ = non-dimensional temperature scaled to a reference.

G = radiative flux $(\mathrm{W/m^2})$.

Subscripts and Superscripts

i = nodal index into beam across thickness.

j = nodal index along beam down length.

c = coating region.

b = beam region.

rad = radiation.

surr = surrounding.

ref = reference.

surf = surface.

1. Introduction

This effort is a thermally oriented design, analysis, and validation study that was necessary in the process of adapting an experimental rig for testing at elevated temperatures. Developed and used by Reed and Pearson to determine the bulk mechanical property of two thermal barrier coatings (TBC); magnesium aluminate spinel ("mag-spinel"), and 8% yttrium-stabilized zirconium (8-YSZ) [1, 2, 3]. The rig was used in room temperature studies. They determined complex modulus for the TBC material under test based using a suspended, free-free, resonating beam coated in the middle 25% of its length with the TBC. Mechanical characterization of such coatings is motivated by the realization that they are very effective at damping high-cycle fatigue (HCF) vibrations relative to the classical alloys used in turbo machinery in both the "hot" and "cold" sections (e.g., turbine and compressor sections, respectively). Reed and Pearson determined that the TBC materials were about 2-3 orders of magnitude more effective than the blade substrate-alloys when compared on a volumetric basis. The design of this rig was the culmination of evolution in technique and design; from the adoption of beams from plates [4], the addition of vacuum to eliminate air damping [5, 6], the

adoption of free boundary conditions to eliminate the large bias errors from clamp-interface damping [2], to non-contact excitation using paired magnets [7], to inferred strain fields from a analytical dynamics solution [8, 9], and from using contacting measurement (piezo accelerometers) to non-contacting measurement (a Doppler velocimetry laser -DVL) [2, 3]. The primary effort was focused on driving out extraneous damping from the rig, and secondarily, adopting a geometry that was analytically simpler and easier to drive to large displacements (e.g., from a plate to a beam).

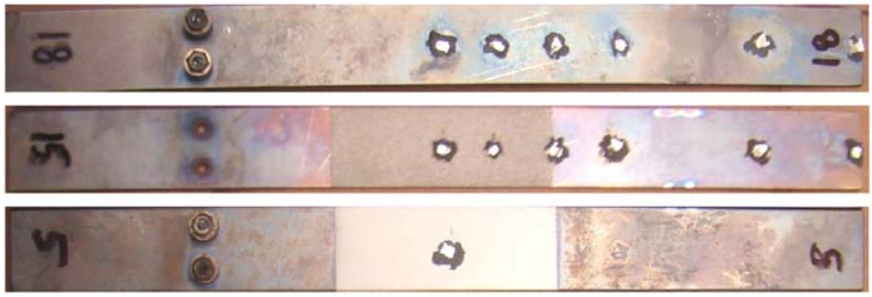

Figure 1. Beam specimens. Free-free beam specimens. Bare (top), bond coat only (middle), and coated beam specimens (bottom). Active nodes with permanent magnets are to left. Beam is 8.0” long.

Figure 1 shows some specimens and Figure 2 is a photograph of the room temperature rig Reed used. The specimens are thin beams about 0.2m in length machined from titanium. The top specimen in the figure is a bare beam and the middle one is bond coated with NiCrAlY blend. This bond-coat layer is very rough and discontinuous; they are applied to prevent loss of the TBC layer from disbanding with mechanical fatigue. The bottom specimen is a fully coated beam with TBC applied over the bond coat by the air plasma spray (APS) process. The TBC is applied to each side of the beam to varying thicknesses. The cylinders in the photo, located about $2/5^{\text{ths}}$ down the length of the beam, are permanent magnets, in this case, aluminum-nickel-cobalt (ALNICO), clamped to the beam with fine machine screws. The dots are mica tape reflectors to aim

a Doppler velocimeter laser (DVL) upon the specimen. Since the beam is excited into the fundamental mode of bending (Bending Mode-I), the magnets and suspension wires are placed at the zero-displacement node lines, while the DVL reflector dot is placed in the center where a large range of displacement occurs.

As seen on the left hand side of Figure 2, the beam is suspended vertically and centered over an electromagnet. This provides the excitation to the beam in a non-contacting fashion. Dynamic response of the beam is used to assess coating materials such as 8-YSZ or aluminum magnesium spinel ("mag-spinel"). The response of the beam system can be measured by either a free-decay or forced-response methodology, Reed and Pearson have obtained results from both approaches. Key features of this rig in regards to the dynamic measurements are non-contacting excitation, measurement, and a (minimal contact) free-free hanging boundary condition on the beam specimen. Determination of the field variables of strain is achieved by using a modal solution obtained from a finite element analysis (FEA) model scaled to the experimental system. This avoids disturbance of the specimen from directly-bonded strain gages. These features kept parasitic energy losses to a minimum and the damping of the system repeatable across trials and rig setup. Complex moduli obtained have been repeatable with little bias error introduced by clamps, excitors, and strain measurement devices.

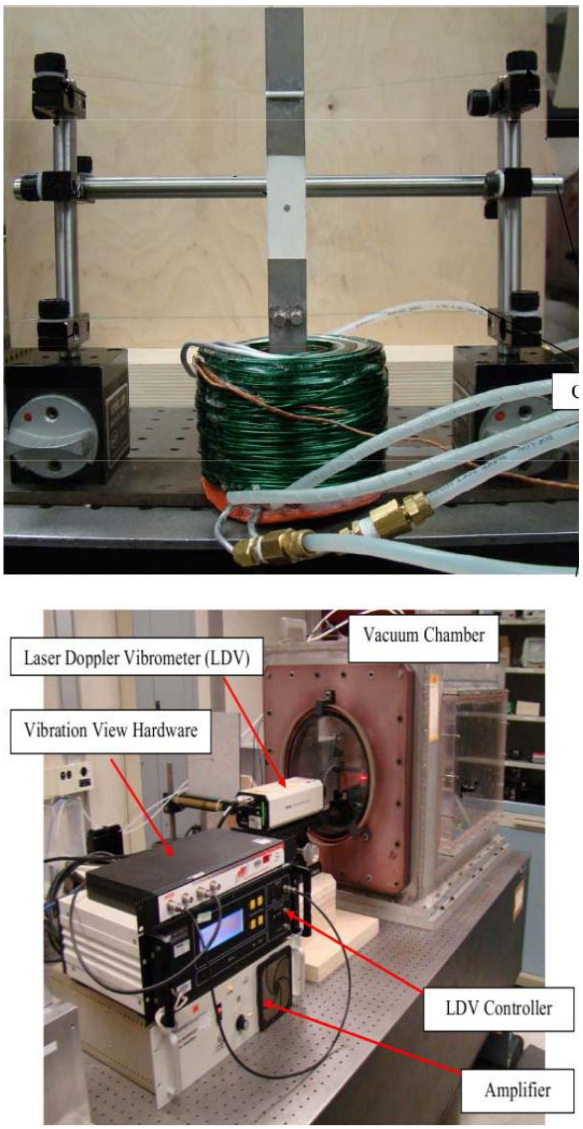

Figure 2. Free-free apparatus (left). Free-free beam specimen suspended from the upper bending mode-I anti-node and with rare earth magnets attached to the lower anti-node. Green mass is the electromagnet used for excitation. Rig inside vacuum chamber (right).

The findings by Reed and Pearson show that TBC's have the ability to absorb high-cycle fatigue (HCF) much more effectively than classical metallic alloys, some 2 to 3 orders of magnitude more effective when compared on a per-volume basis to a common alloy of titanium frequently employed in turbo-machinery cold sections, Ti-6AL-4V [2, 3]. Realization of this damping effectiveness drives motivation to study their behaviour in environments encountered in modern turbo-machinery "cold" sections. In modern 40:1 operating pressure ratio (OPR) engines, this leads to air temperatures of around 500degC in the innermost compressor stages resulting from adiabatic compression [10]. Fortuitously, this also is around the maximum working temperatures of the highest temperature class of magnets, ALNICO magnets. While adapting the rig to high temperature studies, several characteristics of the Reed rig were deemed worth preserving: Non-contact excitation, non-contact velocity measurement, and the non-contacting boundary conditions of the free-free suspended beam. These, along with the extrapolation of strain values from the FEA models that assume the mode shape of the beam, results in a system with very little energy loss resulting from disturbances. Though the rig cannot achieve modern turbine inlet temperatures (in excess of 1100-1300degC), being limited by the Curie temperatures of the ALNICO magnets, it is felt that determining the TBC behaviour on compressor substrate materials at compressor temperatures is worthwhile.

Since the beam is a tuned resonance system, it was critical to ensure the stiffness remains uniform with the exception of the TBC region. The modulus of titanium Ti-6AL-4V alloy varies considerably with temperature [11, 12], and thus maintaining the beam at a relatively uniform state at each temperature condition imposed is important. The Young's modulus of Ti-6AL-4V varies from 115.0GPas at room temperature (approx 298K) down to about 70.0GPas at around 755K (900degF); this was determined using this rig upon population of bare beams. One widely cited source, MIL-Handbook-5H, reports values

somewhat above these measured ones at elevated temperatures [11]. Significant temperature gradients within the beam would drive a non-uniform stiffness variation in the beam, resulting in excursion of the experiment from the bending mode-I tuned resonance in the FEA model in both shape and frequency. Also, significant thermal gradients within the coating would drive indeterminate values for the coating loss and storage modulus values as the temperature field would be unknown and variant. The definition of "near-isothermal" was determined to be ± 10.0degC. This ensures no more than about a 0.75% modulus variation from that intended at the temperature set point. Though this seems like a small variation in modulus, the tuned resonance frequency peak of the bare beam can wander a significant amount with such a small variation, on the order of 0.20Hz. Since the Reed rig has such a high quality factor $(Q \approx 2{,}500)$, a very sharp resonance peak results and such variation can slide the whole peak off the set-point. Many modifications in the design, made to harden the rig's components to higher temperature testing, also drove the inherent damping introduced by it even lower. Quality factors as high as 12,500 were obtained. Such high sensitivity drove the need for a detailed thermal analysis and study of the temperature field within the beam.

2. High Temperature Design and Requirements

The current design, intended to test temperatures of around 500degC, suspends a 0.203m long by 19.050mm wide beam of 1.5875m thick (8.0in × 3/4in × 1/16in) Ti-6AL-4V. This alloy was chosen as it is one in predominate use within turbo-machinery compressor sections. As seen from Figure 1, the coating under test is applied to both sides over the center 25% of the length of the beam to a thickness of from 0.154 to 0.308mm (6 to 12 mill-inches ("mils")) depending on the depth of coating desired. This partial length configuration, known as a partial, modified Oberst beam, ensures a near-constant strain field down the length of the

coating as the beam undergoes bending [13]. The layer of NiCrAlY bond coat, about 0.025mm (0.001in) in average thickness (it is highly irregular in profile), is underneath the top layer to enhance the adhesion of the TBC to the beam substrate.

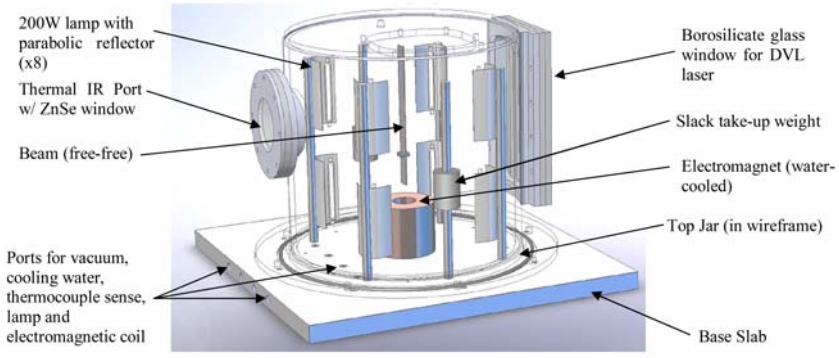

Figure 3. Chamber design. Solid works model of the chamber design cutaway. Outer pressure vessel is indicated by wire frame outline. (Note: radiation shields, wires, and coolant tubing are not shown in this drawing for clarity.)

As seen from Figure 2, there is a single suspension line, consisting of 0.004in diameter nichrome wire that runs through a hole, 0.2032mm (0.008in) in diameter, that is plunge electrostatic discharge milled (EDM) through the neutral plane of the beam at the location of the upper node. From this single wire, the beam hangs. A pair ALNICO magnets consisting of 3.175mm (1/8in) high cylinders by 6.35mm (1/4in) in diameter are clamped to the beam with a single fine threaded machine screw. The N-S poles run along the centerline axis.

The design in Figure 3, shows the rig used by Reed and Pearson modified for higher temperature testing. The specimen is enclosed within a low-vacuum chamber fashioned from AL-6061, with a top jar and a base-plate. Vacuum of around 7.5-9.0torr was maintained during testing for a dual function: First, to eliminate air-damping, and second, help to maintain an isothermal beam. Power for the lamps and magnet, signal

wires for thermocouples, a vacuum port, and cooling water for the magnet were routed through ports in the base-plate. The top jar, shown in wireframe in the figure, provided two optical access windows into the beam one was a rectangular window with borosilicate glass of 3/32in thickness that runs the length of the beam to allow DVL measurements along its entire length. The smaller, circular port was an infrared transparent (IR) window with a zinc-selenide window (ZnSe) to allow thermal imaging of the interior chamber. About 6.35mm (1/4in) thick, it was manufactured by Phoenix Technologies. Eight halogen lamps of 200W each were located in a polar array of two lamps end-to-end around the beam, these provided the power to radiantly heat the beam. Each lamp was located at the focus line of a parabolic trough reflector, which were aimed at the centerline of the beam. The whole chamber interior around the lamps and beam were enclosed with triple layer aluminum foil shielding. This radiant shielding thermally isolated the beam, reflectors, and lamp bulbs from the other interior components like the electromagnet, wires, and coolent tubing. The electromagnet, the hollow cylinder below the beam in Figure 3, which remains below the beam, is cooled by pumped water. It is a temperature sensitive component as the insulation in the magnet wire that would break down under the heat from the lamps. Further details of the design and construction of the high temperature rig are available in the reference [12].

The beam is suspended within the center of the vacuum chamber, surrounded by the radially symmetric array of linear halogen lamps, eight in all, to maintain a near-uniform illumination on the beam specimen. The base plate, like the chamber walls, is fabricated out of aluminum 6061, features a main axial silicone o-ring seal. Similar seals are used in the optical ports; silicone was chosen for the static glands as this particular material has the highest service temperatures among the common elastomeric seal materials. Many of the components in the original setup had to be adapted and/or changed out for high temperature use [14, 15, 16].

3. Numerical and Analytical Studies

The heat transfer aspect of this design was critical to the success of the rig for two key reasons. First, the beam must remain in a near isothermal state in order to ensure that the bending stiffness is constant down the length; second, the temperature versus illumination power curve needs to be determined in order to allow control over this parameter. In addition, this analysis was to determine if the power requirements will be reasonable, and the temperatures encountered in the rig will be safe for components and the operator and meet the design range goal. So, a lot of focus was given to heat transfer analysis of the design. Comparative studies included the following: A non-dimensional analysis, a 1-D analytical solution, a 2-D finite difference numerical solution, and a 3-D FEA analysis. Literature has little on the details of non-dimensional analysis or finite difference modelling with radiation boundaries hence they are covered herein. Experimental verification of the designed chamber was also accomplished by means of thermocouple measurements as well as by infrared (IR) imaging.

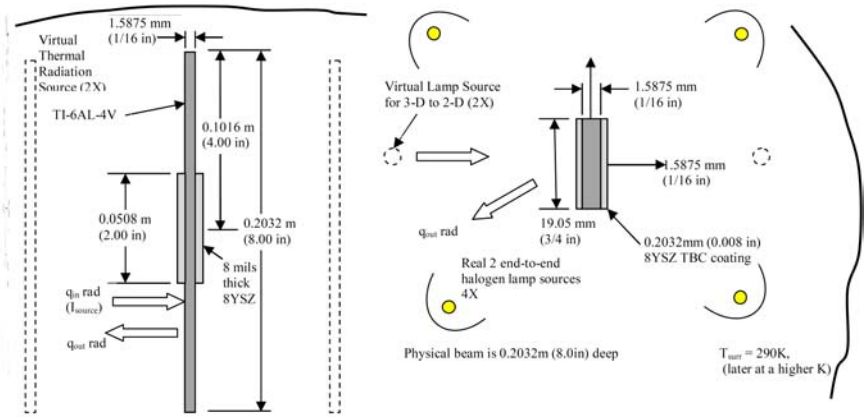

Figure 4. Heat transfer problem. Left, is side view of the beam and Right, is view from above the beam.

Figure 4 is a schematic of the thermal problem under study from the side- and top-view. The real illumination sources, indicated by circles within the arc reflectors, are the four sets of lamps (with two bulbs aligned end-to-end) located around the beam. For the 2-D analysis of the problem using a finite difference code, these four real sources were replaced by two virtual sources. This was felt a reasonable assumption provided the polar array was radial symmetric around the center of the beam and that the real sources where sufficiently far removed from the beam. This latter assumption was to ensure a near-uniform irradiation intensity from the directly emitted light arriving at the beam face. End dispersion effects from the lamps were ignored. The beam and lamps are within a surrounding environment that is at an assumed temperature. All convective transfer within the surrounding vacuum is negligible, the only heat exchange is conduction within the beam-TBC solid and radiation between the bodies. From this problem setup, both an analytical and numerical study were performed to determine the feasibility of the design.

3.1. Analytical

Since this is intended to be a lumped-capacitance serial radiation-conduction thermal circuit, the first effort was to perform an analogy study between a serial convection-conduction circuit and one adapted to the rig. Surprisingly, rather lengthy literature search was required to find mention of the Stark number (St), sometimes known as the "radiation Stefan" number, which is the analogous to the reciprocal of the Biot number (Bi). The Stark number characterizes a serial convection-conduction circuit [17, 18].

Conducting an analogous dimensional analysis on the serial radiation-conduction circuit, using Equation (1), which is the well-known serial conduction-convection circuit Biot number as a guide

$$Bi = \frac{R_{cond}}{R_{conv}} = \frac{\frac{\Delta x}{kA}}{\frac{1}{hA}} = \frac{h\Delta x}{k}, \tag{1}$$

the Stark number for the beam system can be determined as

$$\frac{1}{Sk} = \frac{R_{cond}}{R_{rad}} = \frac{\frac{\Delta x}{kA}}{\frac{1}{h_r A}} = \frac{\frac{h_r \Delta x}{kA}}{1 / \varepsilon\sigma A\left(T_{surf}^2 + T_{surr}^2\right)\left(T_{surf} + T_{surr}\right)}, \tag{2}$$

where the values of characteristic length (L_c) and radiation surface coefficient (h_r) are defined as per

$$L_C \equiv \frac{V_{body}}{A_{surface}};$$

$$h_r = \varepsilon\sigma\left(T_{surf}^2 + T_{surr}^2\right)\left(T_{surf} + T_{surr}\right). \tag{3}$$

When Equation (3) is evaluated in a worst-case scenario where a 755.4K (900degF) beam specimen is within a surroundings temperature of ambient (about 293.2K (68degF)), the reciprocal of Stark number is around 0.000025, which is well below 0.1, the oft-cited threshold of validity for utilizing lumped capacitance with a conduction-convection system. Later, after refinement of the rig design, the Stark number reciprocal was determined to be around 3.8×10^{-5}. This was because the surroundings of the beam now consisted of very hot layers of radiation shielding (multi-layer foil) that were at about 644.3K (700degF). A high Stark number indicates a radiation conduction lumped capacitance situation applies.

A more sophisticated analytical model of the beam was performed inspired by boundary-layer theory. The setup of the analysis, assumed the beam was suspended in a uniform imposed thermal radiation field of specified flux intensity, I (in $\mathrm{W/m^2 \cdot deg\ K}$); convection was assumed to be negligible. Assumptions included: a uniform irradiation surrounds the beam, the beam's length is much greater than the width, which is subsequently much greater than the thickness (e.g., $1 >> w >> t$) the TBC coating patch is negligibly thick relative to the beam ($t_c << t_b$) and

is a surface property variation only, and that the beam is homogeneous and isotropic with regards to thermal conductivity. It was felt that a uniform field of radiant energy was a reasonable assumption provided the eight lamps were in a radially symmetric array and were sufficiently far removed from the beam to allow for the cylindrical flux surfaces to be only slightly curved at arrival at the beam face. By employing a boundary-layer-inspired assumption, in which the one significant temperature gradient was along the long axis of the beam, the 3-D conduction problem was reduced to a 1-D one. Using non-dimensional quantities in this ODE and performing a simple perturbation expansion upon the ordinary differential equation, a temperature distribution as a function of location down the beam length was obtained. Details on the development of this solution are presented in the research summary covering the development of this rig [12].

It is noted that the rearrangement of the Stefan-Boltzmann equation, as given in Equation (4), gives a good surface temperature approximation in high Stark number situations based on the impressed radiation, I, and the temperature of the surroundings, T_{surr} with a steady state system

$$T_{surface} = \sqrt[4]{\frac{I}{\sigma} + T_{surr}^4}. \tag{4}$$

3.2. Numerical analysis

Numerical simulation of the beam was performed for a steady state solution by two methods; one a 2-D finite difference model using a Matlab code and the other was a 3-D finite element analysis performed using Abaqus v6.8-2, commercial code [19]. Both of these simulations were performed with three goals in mind: (1) to determine the target temperature field that the beam-TBC system would reach as a function of the experimental parameters (illumination source power and distance, emissivity's of the titanium and TBC, surroundings environment etc.); (2) whether a near-isothermal state would be achieved in the beam and TBC regions, preserving constant beam stiffness and avoiding large property

variations caused by thermal gradients; and (3) allow parametric design studies to be performed on the beam chamber design. The third point involved investigation of lamp failure impacts, reflector geometries and aberrations from the ideal, and varying the heat source distance(s) from the specimen. The finite difference code featured a rectangular nodal grid 9 × 26 in size. The grid was non-uniform in the direction of depth into the thickness and is depicted in Figure 5. This was in anticipation of steep thermal gradients being located within the ceramic layer. A 2-D computational planar slice in the mid-span of the width (at $w/2$) was anticipated to be adequate, as the beam's width is much greater than the thickness ($w >> t$). Thus, minimal heat flow would occur in the third (width-wise) dimension with the plane sufficiently removed from the edges. A half-domain grid was used with the symmetry plane treated as adiabatic. Adapted from a code developed to model a Hall-effect thruster by Bohnert [20], the code utilized the Laplace heat conduction equation within the solid regions of the beam and TBC. A rule-of-mixtures approach was applied where the finite difference volumes spanned the interface between the metallic beam and TBC ceramic materials. Thermal contact resistance between the metallic beam and the TBC was assumed to be negligible.

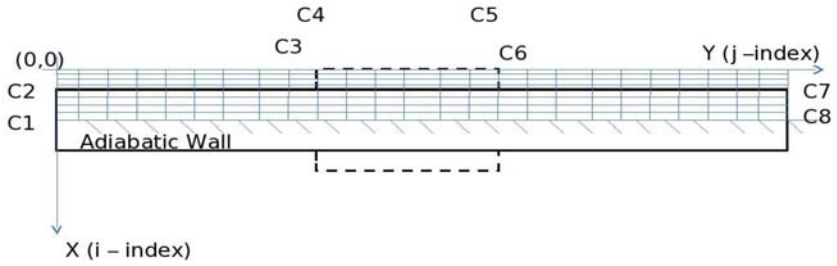

Figure 5. Finite difference grid. 9 × 26 non-uniform (on beam thickness coordinate) nodal grid.

At the boundaries between the solids and the vacuum, the Stephan-Boltzmann law was applied in a conservation form with irradiation of specified flux (I) being impressed on the solid surface with the conduction occurring to the surrounding solid nodes in a radiative-conductive finite difference equation. Being fourth-order with respect to the nodal temperature, and therefore highly non-linear, two possible means to allow handling the nonlinearity were considered. The first was to utilize localized convergence at each node, where the I was imposed on the initial nodal temperature $(T_{i,j0})$ and the updated temperature assessed $(T_{i,j})$. This allowed a reassessment of the flux conditions, and iteration within the node proceeded to occur using $T_{i,j0}$ until a convergence criterion was met before proceeding to the next node. The second technique, this one employed in code developed, was to locally linearize the radiative conductive finite difference conservation equation around the $T_{i,j0}$ and solve for the updated temperature $(T_{i,j})$ from this linearized equation. Running iterations of the whole domain out a sufficient amount allowed global convergence and the non-linear flux conditions to assert themselves. Using Figure 6 as a sample control volume, the conversation of energy applied to the finite difference volume with the impressed radiation, re-emission, and conductive exchange with the three neighbouring nodes works out as

$$q_{in} = 0 = \frac{k\Delta x(1)}{2\Delta y}\left(T_{i,j+1} + T_{i,j-1}\right) + \frac{k\Delta y(1)}{\Delta x}\left(T_{i+1,j}\right) - T_{i,j}\left(\frac{k\Delta x}{\Delta y} + \frac{k\Delta y}{\Delta x}\right) + I\alpha\,\Delta y(1) - \varepsilon\sigma\,\Delta y(1)\left(T_{i,j}^4 - T_{surr}^4\right), \quad (5)$$

where energy into the node is treated as a positive flow. Locally linearizing the influx of radiation around the current nodal temperature, $T_{i,j0}$, and expanding the first two terms yields

$$q_{in\ linearized} \approx \varepsilon\sigma(\Delta y)(1)\left(T_{i,j}^4 - T_{surr}^4\right) = q_0 + \frac{\partial q_0}{\partial T_{i,j}}\left(T_{i,j0} - T_{i,j}\right)$$

$$= \varepsilon\sigma(\Delta y)(1)\left(T_{i,j0}^4 - T_{surr}^4\right) + 4\varepsilon\sigma(\Delta y)(1)\left(T_{i,j0}^3\right)\left(T_{i,j0} - T_{i,j}\right). \quad (6)$$

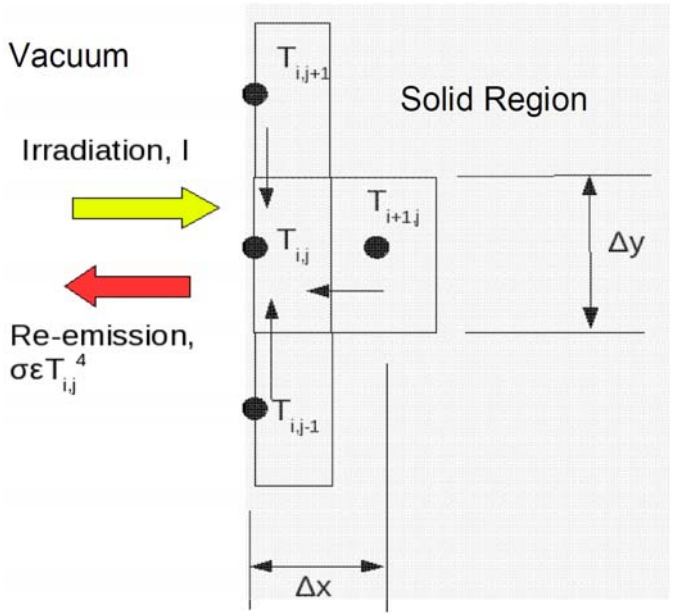

Figure 6. Nodal control volume. A typical surface nodal control volume in with a Stefan-Boltzmann surface boundary condition.

Replacing q_{in} in Equation (5) with the expression in Equation (6), one obtains

$$q_{in} = 0 = \frac{k\Delta x(1)}{2\Delta y}\left(T_{i,j+1} + T_{i,j-1}\right) + \frac{k\Delta y(1)}{\Delta x}\left(T_{i+1,j}\right) - T_{i,j}\left(\frac{k\Delta x}{\Delta y} + \frac{k\Delta y}{\Delta x}\right) + I\alpha\Delta y(1)$$

$$- \varepsilon\sigma\Delta y(1)\left(T_{i,j0}^{4} - T_{surr}^{4}\right) + 4\varepsilon\sigma\Delta y(1)\left(T_{i,j0}^{3}\right)\left(T_{i,j0} - T_{i,j}\right). \qquad (7)$$

Equation (7) is now linear with respect to nodal temperature, $T_{i,j}$, which is the value that is solved for in the current iteration through the nodal grid.

The assumptions inherent in the simulation included the gray surface assumption, where absorptivity equals emissivity ($\alpha = \varepsilon$), a steady-state solution applies, and that convective transport in the vacuum around the beam is negligible. The TBC was modelled with an emissivity of 0.45 while that of the Ti-6AL-4V alloy is 0.23.

The code was subjected to validity checks, these included: that a unique solution field convergence occurred regardless of the initial temperature field, grid density independence with 4× the nodal density, and the meeting of a global convergence criteria. The typical results of a simulation run to model the beam/TBC system is displayed in Figure 7. It is noted the field converges to a near isothermal state as predicted by Equation (7). The figure shows that the ceramic layer's differing thermal conductivity and emissivity has little impact on the thermal uniformity in the beam specimen.

The finite difference code was considered to have converged by about 30,000 iterations; a calculation of the difference of the average temperature field in the metallic and coating domains between successive iterations, defined as $\varepsilon = (T_{ave\,I} - T_{ave(i-1)})/T_{ave(i-1)}$, was about 1.0×10^{-8} out at 2M iterations. The code raised issues with design of the chamber, even with a very strong illumination of the beam at 10× the solar constant, the beam could only reach around 433degC (812degF), this suggested the need for a redesign to add radiation shielding.

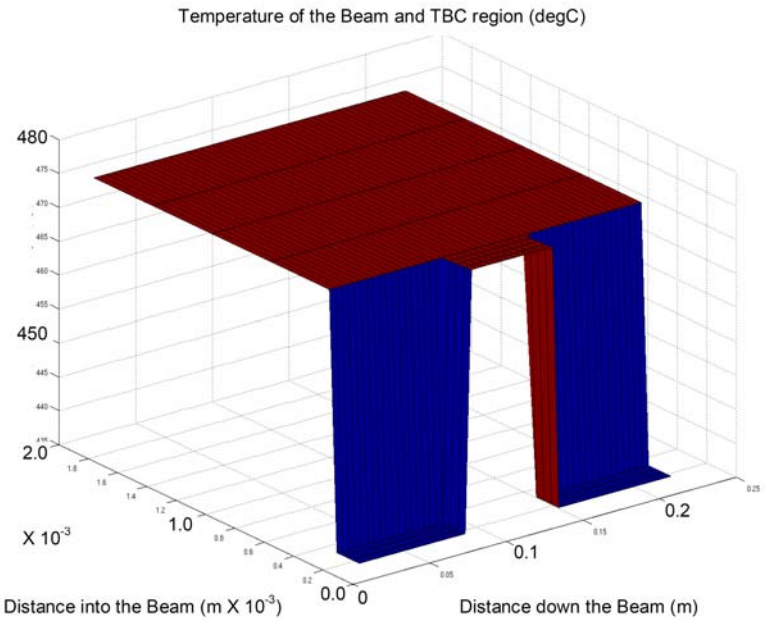

Figure 7. Surface plot of converged finite difference temperature field. Field is isothermal at around 475degC of the half domain. Notched region at lower right is the TBC-coated region in the middle 25% of the beam length.

The final 2-D FD runs were performed with a 644.3K (700degF) blackbody surroundings, as determined from preliminary heating testing of the chamber with shielding installed, and an imposed radiation of $I = 6850\text{W/m}^2$, this was derived from 15.24cm (6.0in) long lamps over the 20.32cm (8.0in) long beam back calculated from 5× the solar constant $(1370\text{W/m}^2 \times 4.0)$. This resulted in a near isothermal beam at around 749.8K (890degF) close to the intended design max at 755.4degK (900degF).

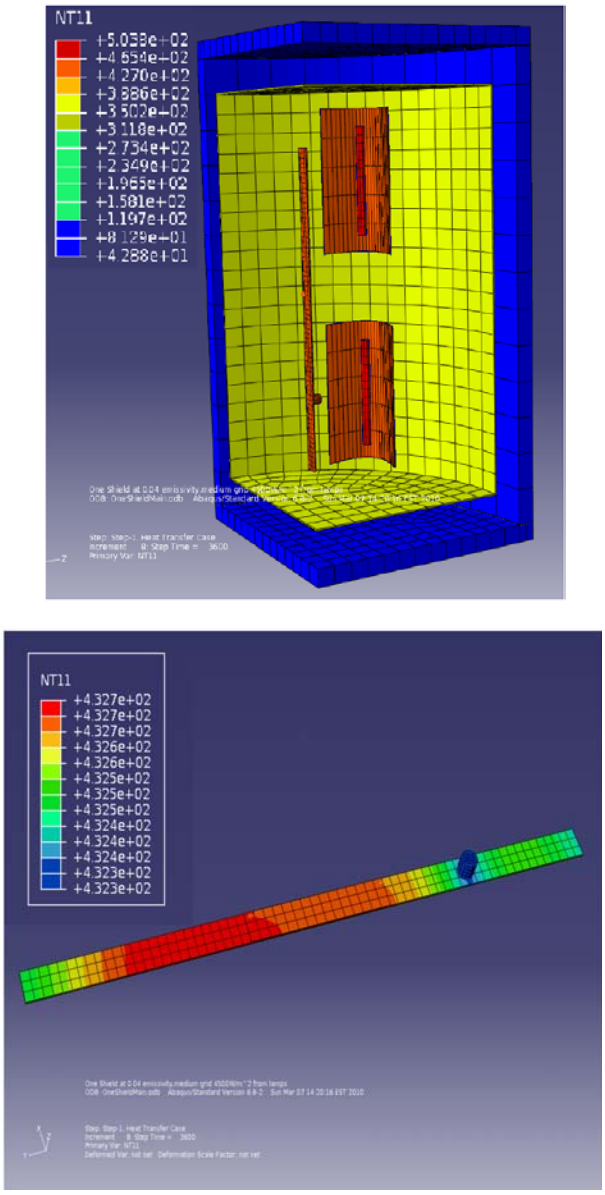

Figure 8. Finite element analysis results. Left, global results for the chamber including beam, outer walls radiation shield, reflectors, Right, close up of 1/4 piece of the beam (lower edge is the symmetry line across the width).

The last of the heat transfer studies conducted prior to final construction of the chamber, was a 3-D finite element analysis performed. The program's heat transfer capabilities include conduction and radiation thermal transport. A quarter-domain model with two planes of symmetry running through the centerline of the beam and chamber was used. The following components were modelled as solids using the 8-noded, linear shape-function brick heat transfer element: The outer chamber walls, the radiation shield (now added based *i*), the beam with the TBC coating and ALNICO magnets, the lamp heat sources, and the parabolic trough reflectors paired with the lamps. Figure 8 on the left side, displays the quarter model of the system, while the right is the beam alone. The mesh density of the beam was chosen to match the mesh used by DeLeon [13] 12 in his dynamic model. Sensitivity studies as well as optimal selection of the incompatible element were performed by this author [13]. Adherence to this model was felt important should a coupled thermal-stress model be required. Mesh density at 2× and 1/2× density along with initial condition temperature fields were performed and found not to influence the final converged solution. The elements used were the standard 8-noded continuum element for scalar fields (Abaqus "C3D8" element).

It is important to note that the radiation modelling in Abaqus assumes the following: diffuse emission and reflection, gray surfaces, and that Kirchhoff's radiation law applies [21]. The emissivity's modelled for the beam were the same as in the FD code, while that of the radiation shield was 0.04, a commonly cited value for aluminum foils, the interior of the chamber walls was set at 0.12, common for weathered aluminum finish [22]. The ALNICO magnets with a black oxide finish were modelled with $\varepsilon = 0.8$. Newton's law of cooling was applied to the exterior walls of the chamber, with the free convection coefficient of $1.0 \mathrm{W/m \cdot degK}$ on the top- and bottom-lids and $10.0 \mathrm{W/m \cdot degK}$ on the cylindrical wall. These are common values cited for free convection in quiescent air, in this case at 298K [23]. Meanwhile, the inside of the

chamber is in a vacuum so there is no convection. The lamp glass bulbs were treated as blackbodies ($\varepsilon = 1.0$) of a specified temperature. Validation of the model was checked for mesh density independence, convergence from differing initial conditions, and checking for global energy conservation [12].

Figure 8 right shows the thermal gradients within the quarter-beam with the coating and magnets. It is important to note that the isotherm color band range is set from 432.3degC to 432.7degC, and as a result the whole beam is essentially isothermal. The very slight gradient that is apparent may be from the magnet providing a cold spot from which heat is radiated out to the (colder) surrounding shields. It is worth noting that the radiation shield reaches a temperature of around 645K (700degF), the outer walls remain around 310-320K (100 to 115degF).

The conduction within the solid bodies, as well as the outer-surface free-convections, are governed by Newton's law of cooling and as a result are all linear in nature. However, the radiation exchange within the cavity is non-linear, and for this the Abaqus defaults were accepted. These conditions are: There is a zero heat flux condition upon convergence relative to the time-averaged heat flux; to be less than 1.0×10^{-5}, and a convergence criteria for the residual heat flux is when there is a zero flux that is less than 1.0×10^{-5}. The surface flux at the beam, back-calculated from the lamps to arrive at a near 755.4K (482.2degC/900degF) field within the beam is about $4{,}500\text{W/m}^2$ at the surface of the beam.

The simulations were performed with the lamp bulb glass surface treated as a fixed temperature boundary, the Stefan Boltzmann law was used to obtain the glass temperature (T_{glass}), knowing the power supplied to the lamps (E), and the area of the bulb surface (A_{glass}), as per

$$T_{glass} = 4\sqrt{\frac{E_{bulb}}{\sigma \varepsilon A_{glass}}}. \tag{8}$$

An alternative could be to impose boundary conditions of flux (Neumann-style) at the lamp bulb surfaces, but the solution time of the non-linear radiation cavity is substantially higher as determination of the thermal source temperatures are now floating. Blackbody emission from the glass bulb envelope surface was imposed, as opposed to the finely coiled filament surface. There was a two-fold reason for this, first, it was easier to measure the surface area of the bulb glass, and second, the elements formed by meshing of the bulb glass were much better formed and a coarser grid. This allowed not exceeding the degree of freedom limitation in the commercial code. This would be impossible on the fine wire of the filament. There is a 16,000 participating node limit in the cavity-exchange network; this is to avoid trying to solve an excessively large non-linear system [21]. Based on observations drawn from work with a thermal camera system, it was concluded the glass envelope was infrared opaque to the filament emissions and coupled with the assumption of frequency independent emissivity and absorptivity, this was a reasonable modelling assumption.

The FEA analysis yielded much insight into the rig design. It clearly indicated again that a high Stark number environment was in effect. Examination of Figure 8, right, on the close-up of the beam shows the lack of color-band (temperature) changes occurred when traversing the beam along the depth or width. Only the length exhibits temperature gradiant and this is small relative to the bulk temperature changes imposed. This validates the boundary-layer inspired simplification in the analytical solution. Another key design modification motivated by both the FEA and FD codes was the necessity to add a layer of multilayer shielding around the inner core of the chamber with the lamps, reflectors, and the beam. This was manifested by the excessively high temperatures in the outer chamber walls as well as excessive power requirements needed by both model(s) to achieve the target design temperature maximum of 482.2degC (755.4K/900degF). Coupled with the need for the multilayer foil shielding was a design decision to increase the bulb wattage as well to 200W per bulb (1.6kW total).

4. Experimental Setup and Realized Design

Based on the insights gained from the heat transfer studies, the apparatus was fabricated. The conceptual design as shown in Figure 3 was implemented with some minor modifications. Chief among these was the addition of a triple-layer foil radiation shielding layer that enclosed the beam, lamps, dummy specimen, and lamp reflectors. Lamp power was doubled from 100W to 200W each. The dummy beam specimen is a static beam specimen that is equipped with thermocouples bonded to it to allow measurement of the beam's temperaure. The dummy has the same geometry as the beam and is suspended so as not to interfere with the thermal or mechanical aspects of the dynamic specimen. The bias error between the dummy beam temperature and the dynamic free-free beam temperature was determined to be within 0.3degC based on workup testing [12].

Figure 9. Free-free beam test chamber – interior and exterior views. Left, top-down view of electromagnet prior to specimen placement and lamps and reflectors installation, and Right, an exterior view of the chamber during heat testing. Note: the thermal shielding is not installed in the left view.

Figure 9 is a photo of the chamber interior from the top (left), and the outside exterior of the rig (right) through the laser window. At the bottom of the chamber, and centered within it, is the electromagnet that features twin, large-bore copper cooling tubing wound into the magnet wire. The

four rods around it each have two lamp holders equipped with cylindrical quartz-envelope bulbs measuring 7.93cm (3.125in) length by 0.952cm (0.375in) diameter with end terminals (Cat #: Q200T3/S). Each bulb sits at the focus of a parabolic trough reflector with an aperture opening about 10.16cm (4.0in) wide and is aimed at the centerline of the beam. Ignoring end-dispersion effects and diffusivity of reflections, 50% of the radiation from each lamp is emitted directly towards the beam and features a cylindrical wave-front flux surface, while the other 50% is reflected off the trough and is a constant flux intensity wave front (e.g., planer). The lamps are powered on two parallel branch circuits in a symmetric/anti-symmetric fashion by two variable AC transformers each rated at 0.8kVA that allows setting their power level.

The radiation shielding, which can be seen installed in Figure 10, right, on the sides and lower "floor" of the hot core over the electromagnet and surrounding the lamps, reflectors and beam, consists of three layers of heavy gage aluminum foil, chosen for its high reflectivity. It is also used to line the lamp reflectors. Vacuum is supplied to the chamber through a port in the base slab from a Varion DS301 dual stage rotary vane pump that was able to maintain a steady 7 to 11torr (~0.01-0.015atm) low vacuum in the chamber, thus eliminating both air damping and free convection effects within the chamber [11].

5. Validation Studies

Experimental validation of the heat transfer environment of the chamber was felt critical to ensuring that the rig achieved the design temperature and do so with a near-isothermal beam specimen. Two methods were used, multipoint thermocouples adhered to the beam and a thermal imaging camera system. Ten type K thermocouples (TC) fashioned from 24 gage wire (Omega GG-K-24-SLE, calibrated deviation of 1.05degC (1.9degF) at 400.0degC (752.0degF)). These were routed to an Omega DP-41TC reader via a 10-point rotary selector switch. Figure 10, on the left side, show the locations on the coated beam, where the thermocouple junctions were bonded to the beam, again using the Durabond epoxy. The right side of the figure shows the beam suspended in the rig before closure.

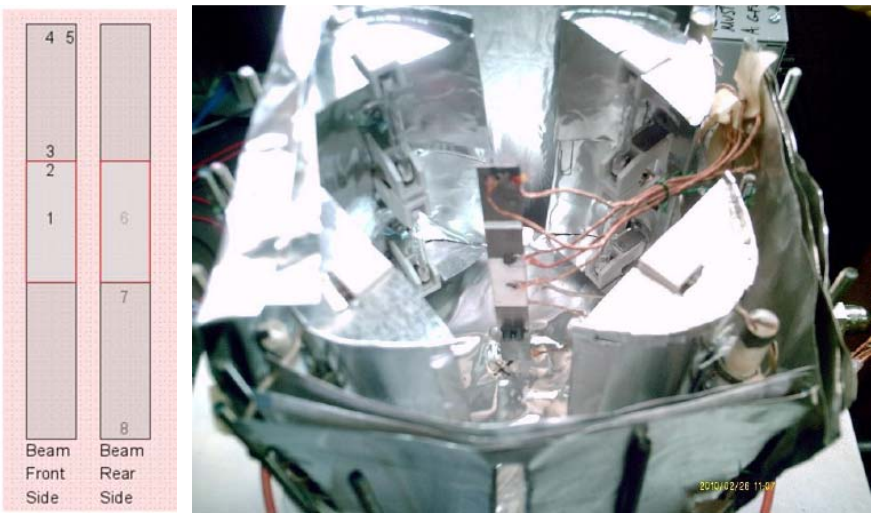

Figure 10. Left, thermocouple channel assignments on the beam, Right, beam in test chamber with K-type thermocouple instrumented beam. All radiation shielding, except the top piece are installed.

The first two heating tests were run with eight 100W lamps set to 100% of their rated power at the onset, and the ten channels were periodically monitored for the thermal response as a function of time. Eight were on the beam, one was embedded within the electromagnet, and the last monitored the room ambient. Figure 11 details the traces of temperature versus time the various TC's. Both run had anomalous results indicated the beam was far from an isothermal state. Upon further inspection, these data anomalies were found to be explainable and correctable. The first heating test as shown by the left plot showed that channels #4 and 5 were depressed below the beam average. These two thermocouple junctions coincided to the top-center and top-corner of the beam. During the test, it was noticed that the beams upper corner was in light contact with the upper layer of radiation shielding. The contact patch area was very small, under 0.25mm^2. Despite this, it depressed the beam temperature significantly in the upper region of the beam. This was a clear demonstration that contact of the beam with shielding must be avoided. A powerful localized cooling path via conduction will form otherwise.

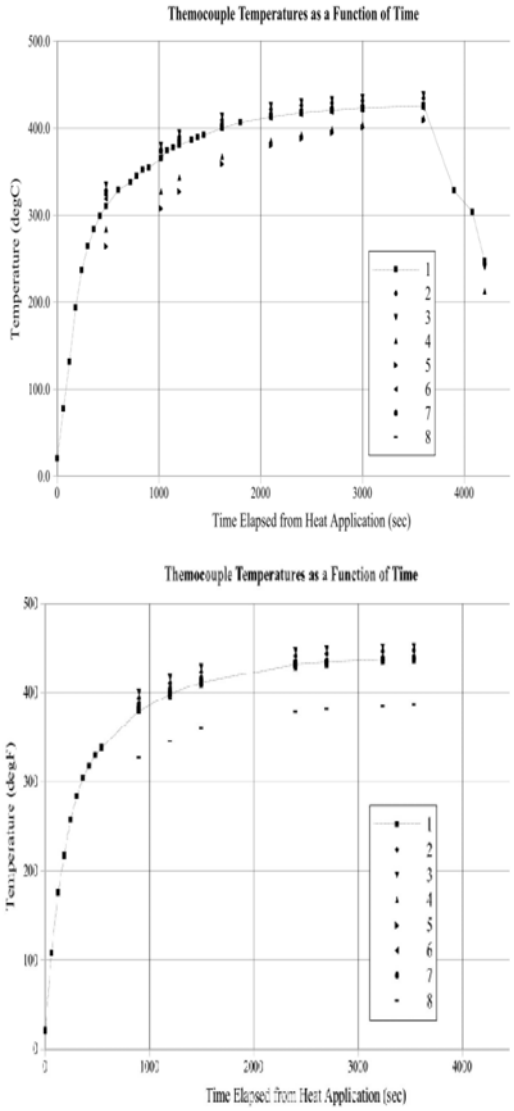

Figure 11. Heating runs on chamber to 100% power (800W total), Left, 1st trial, Right, 2nd trial. Left figure demonstrates the vast localized cooling that can occur is a slight.

The second test, shown in the right plot, with attention being paid to make sure the beam did not contact any other components, now had channel #8 lagging below the rest. Viewing into the chamber showed that

the lower center thermocouple had dis-bonded from the beam due to thermal shock failure of the epoxy. It had come to rest on the lower foil shielding floor and was now registering the temperature of it. The insight gained from this test was used to revise the surroundings conditions for both the FEA and FD models. Based on the failure of the beam average temperature to reach 900degF from the tests (along with the FEA radiation model results), the lamps were doubled in power.

A third test was run with two TC channels now added onto the dummy specimen and used an FLIR SC660C infrared (IR) thermal camera to capture whole-field temperature data. The multi-point thermocouple validation of the chamber had promising results but it was concluded that whole-field thermal imaging of the beam would be more convincing. This system, featuring a 640 × 480 pixel resolution and a 0.04°C(0.074degF) sensitivity and ±1°C(±1.8°F) accuracy, directly measures the radiosity coming from an object [21]. There are some drawbacks to using an IR camera, these include: (1) the camera can image only about half of whole beam as the angle of view from the ZnSe window is small; (2) careful calibration and setup of the camera must be performed; and (3) since the TI metal has a low emissivity it must be coated with to avoid reflection of heat sources and additional sensitivity studies need to be carried out. The details of handling, these are in the references [12, 22].

A 8YSZ partially-coated beam, sprayed with dye-pen entrant developer (Spotcheck SKP-02) on the bare titanium regions, was suspended in the chamber along with the dummy specimen. Each was equipped with two thermocouples. Using eight 200W lamps, the chamber was imaged at 148.88, 315.55, and 482.22degC (70, 300, 600, and 900degF); these were the planned test-points to later evaluate the coatings for their complex modulus. Figure 12 shows the IR image at the design maximum temperature. The beam was also taken to 440.6degC (825degF) in temperature and imaged as well, this was to be used to

compare spatial temperature variation back against the second multi-point TC heating run; these results are later compared. There is little thermal gradient across the beam-TBC interface. Another notable finding is the crocodile clip, used to clamp TC's to the beam, introduces no visible localized cooling in the beam, the clip itself appears colder as it is bare, burnished copper and has a much lower emissivity, about 0.07, than the coating region it is clipped to [22].

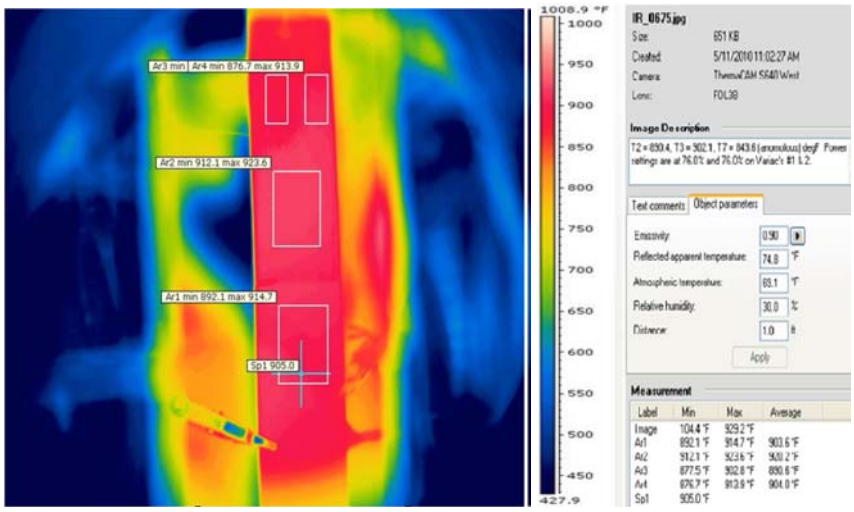

Figure 12. Thermal IR image at 900degF set-point (temperatures are in degF).

The main driver of the difference in measured temperature between the coating and the beam is the difference in the emissivity between the two regions (ε_{TBC} = 0.94 and ε_{TI} = 0.90). As the emissivity calibration of the IR camera is set to the lower-value of the powder-coated titanium, the more irradiative region of the TBC appears hotter as the emissivity is artificially low for this region. One should notice from the thermographic image is the lack of any significant isotherms on the specimen except at the top and bottom edges of the window. This is where diffraction and reflection of light occurs in the IR window and view port walls.

Figure 13 shows the view point of the beam in normal light to clearly show the features in the previous figure. Note that the crocodile clip and TC have been removed. But the remaining features remained the same. As can been seen from the thermocouple wires coming in from the side and their signatures on the FLIR thermo-graphs on the right side of the beam, one can see the aperture angle of the visible light camera is somewhat wider than the FLIR IR camera.

Figure 13. Optical image of beam in chamber from IR camera viewpoint.

A natural question to raise is did coating of the bare regions of the beam with laser developer to eliminate heat source specular reflections from the lamps radically shift the beam's bulk thermal equilibrium temperature away from that of the uncoated state? Also, did artificially closely matching the surface emissivities between the bare and coated regions enforce an isothermal state that was aberrant in nature?

To address these, the FEA model was run with the two bounding cases. All the boundary conditions and material properties were the same for the two cases, except for the emissivity of the bare titanium, which in one case was set to 0.95, representing the developer-coated titanium. For the other case, it was set to 0.10, representing a highly polished beam. The second case is a conservative assumption, as highly oxidized titanium features $\varepsilon = 0.23$ to 0.40. Figure 14 shows the isotherm plots of these two bounding cases, with average temperatures of 431.1degC ($\varepsilon_{TI} = 0.10$) varying about 0.5degC and 432.5degC ($\varepsilon_{TI} = 0.95$) varying about 0.4degC. The global temperature shift is small (about 1.4degC) and isothermality is preserved despite the emissivity change. This is further supporting evidence of the weakness of the influence of surface emissivity variation as concluded from Baker's analytical model [12].

6. Results

The first key result from these analysis and tests was that the range of average temperature in the beam was not meeting the design maximum. With the 100W lamps, the rig was only able to attain about 437.8 to 448.9degC (820-840degF), but replacement with the 200W allowed it to easily reach 482.2degC (900degF); the maximum reached with an excited beam was 565.6degC (1050degF); it may be capable of going higher.

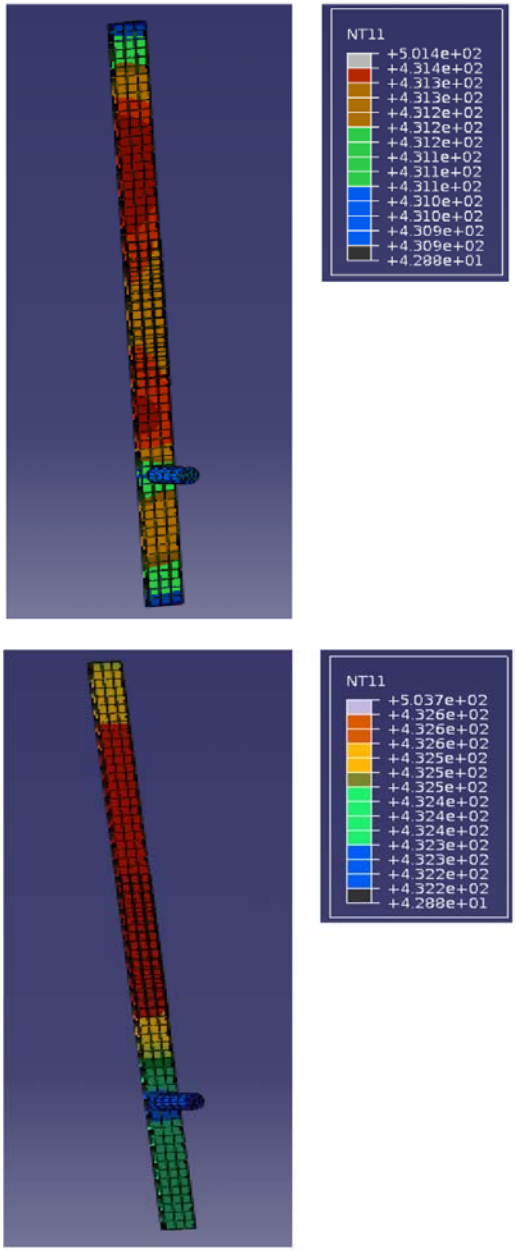

Figure 14. FEA bounding study, Left, highly polished ($\varepsilon_{TI} = 0.10$) and Right, near blackbody ($\varepsilon_{TI} = 0.95$).

The second was finding and validating the temperature distribution in the beam as near-isothermal. The high Stark number environment is indeed a lumped-capacitance problem. Figure 15 is a comparison of the analytical models (analytical solution, FD, and FEA models) with the associated thermocouple and IR-camera measurements of the system. The real data, as realized from the multi-point thermocouple measurements, only exhibit a 15degC variation. This is with the recognition that the very low temperatures of the left-most thermocouple is from the lower foil shielding to the TC epoxy dis-bond. The thermal camera IR temperature range measured, which is over about half of the beam length (due to the limited imaging angle through the ZnSe port), exhibits the same measured variation. This is with the inclusion of the refractive effects that depress the temperature readings at the edges of the window as can been seen with the roll-off at the ends of the measured range.

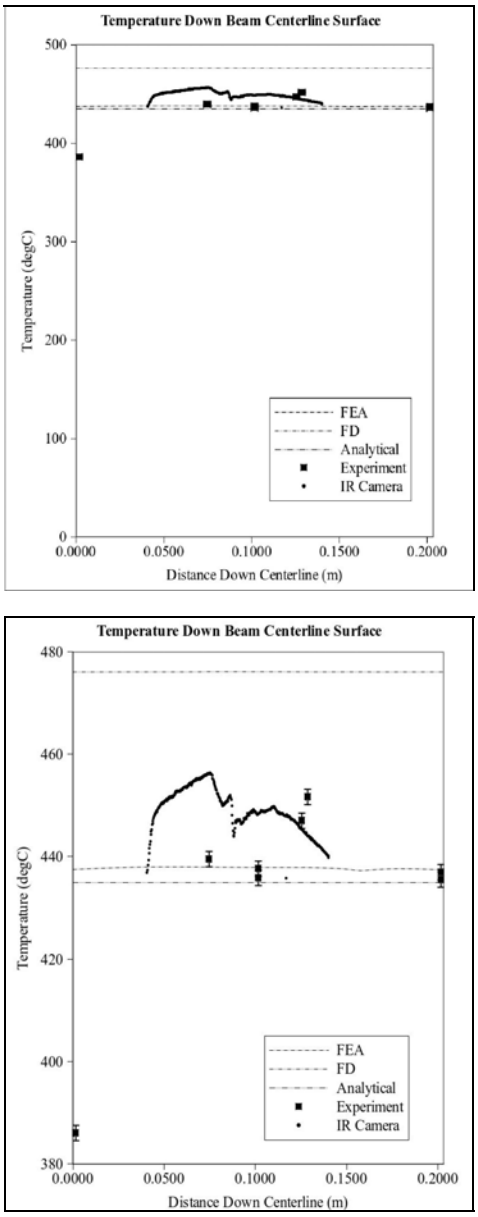

Figure 15. Comparison of temperature findings down the length of the beam, Left is compressed temperature scale and Right, expanded to include room temperature.

Excluding window edge variations reduced the temperature variation to about 10degC throughout the beam. Random variations in the measurement precision, as can been seen from the 0.95CI error bars does not explain all the variation. For the thermocouple measurements, a likely cause of variation in temperature might be the integrity of the Durabond bonding to the beam, variations in the quality of the spot welding, and the local manufacture of TC junctions. (Recall the 2-point thermocouple calibration check placed the TC variations across the population of 10 channels at about ±9.5degF (about ±5.0degC).) These variances aside, others found in the experiment, that are not nearly so pronounced in the numerical models, arise despite the high Stark number of the experimental (high Stark number is a strong radiation-conduction serial thermal circuit that is lumped capacitance in nature) beam and chamber, these include: slight variations in coating emissivity, variation in the lamp's emissive intensity (e.g., bright spots), focal irregularities in the trough reflectors. Evidence of the emissivity variations in the specimen can be seen in the IR camera temperature plot at the beam coordinates of 0.075m and 0.125m, which are the boundaries between the developer-coated bare titanium and the TBC patch the camera exhibits a jump in the readings. If the variations are assumed to be worst-case, where it is assumed where the measurement variations are mainly due to real isotherm variations within the beam, the variation of about 15degC would provoke only a small variation in modulus down the length of the beam. 15degC (27.0degF) corresponds to only about ±0.4GPa of variation in the modulus, about ±0.44% from the value that was determined to be around 91.4GPa at 900degF. Given this fairly small temperature induced variation in modulus of the tuned resonant method on the beading mode-I free-free beam seems a valid assumption with the high Stark number chamber.

7. Conclusion

The novel apparatus and technique introduced by Reed was able to be adapted to allow mechanical characterization of TBC coatings across the range of temperatures, where they may be used in modern turbo-

machinery for suppression of high cycle fatigue in lieu of their primary purpose, that of thermal isolation. With attention to the radiation heat transfer mode, all of the advantages of the room temperature setup were preserved as it was adapted to function in a high Stark number environment. The chamber was found capable of testing free-free dynamic specimens by means of both forced response and free-decay to at least 565.6degC (1050degF/673.2K), and the components proved survivable (lamps, foil, etc) while the beam was near isothermal, preserving its tuned bending resonator mode-I eigenvector (shape) and eigenvalue (resonant frequency).

The damping of the new apparatus was much lower than the rig it was derived from; this was due to a lot of the changes made to harden it to higher temperatures. The natural inclination is to see how truly high the quality factor can climb to reaching the near ideal of a beam vibrating in a zero-g, vacuum environment. Temperature rise will not markedly affect the bending-I mode shape, but the resonance frequency will shift a significant amount; it is suggested that accurate modulus as function of temperature curves be located/determined for the alloys under test.

Recommendations for future effort is to regain some of the strain range that the baseline apparatus was capable of attaining by increasing the size of the electromagnet, lowering the beam into a foil-lined well within the electromagnet bore, and trying samarium cobalt magnets, which feature a relatively high working temperature. Also adding the ability to chill and cool specimens down below room temperature using the chamber would allow simulation of the first couple of compressor stages in a high altitude condition.

Acknowledgement

Finite element modelling assistance was provided by Dr. R. Hoffman of Simulia Systems, Abaqus Division.

References

[1] S. Reed, A. Palazotto and W. Baker, Determining Material Properties of Nonlinear Materials from Transient Response, ASME International Mechanical Engineering Congress and Exposition, IMECE 2007, 11-15 Nov. 2007, 10 PART A, pp. 463-469.

[2] S. Reed, Development of Experimental, Analytical, and Numerical Approximations Appropriate for Nonlinear Damping Coatings, Ph.D. Dissertation, Dept. of Aeronautics and Astronautics, Air Force Inst. of Tech., WPAFB, OH, 2007.

[3] L. Pearson, Vibration Analysis of Commercial Thermal Barrier Coatings, M.S. Thesis, AFIT/GAE/ENY/08-J05, Graduate School of Engineering and Management, Air Force Institute of Technology (AU), Wright Patterson AFB, OH, 2008.

[4] F. Ivancic, The Effect of a Hard Coating on the Damping and Fatigue Life of Titanium, M.S. Thesis, AFIT/GAE/ENY/03-12, Graduate School of Engineering and Management, Air Force Institute of Technology (AU), Wright Patterson AFB, OH, 2003.

[5] K. Allen, Evaluation Techniques for Determining Damping Mechanisms on Titanium Plates, M.S. Thesis, AFIT/GAE/ENY/05-M01, Graduate School of Engineering and Management, Air Force Institute of Technology (AU), Wright Patterson AFB, OH, 2005.

[6] D. Lee, Evaluation of Factors Contributing to Damping of Coated and Uncoated Titanium Plates, M.S. Thesis, AFIT/GA/ENY/06-M06, Graduate School of Engineering and Management, Air Force Institute of Technology (AU), Wright Patterson AFB, OH, 2006.

[7] T. Hoover, An Electromagnetic Tool for Damping and Fatigue Analysis, M.S. Thesis, AFIT/GSS/ENY/04-M04, Graduate School of Engineering and Management, Air Force Institute of Technology (AU), Wright Patterson AFB, OH, 2004.

[8] S. Patsias, C. Saxton and M. Shipton, Hard damping coatings: An experimental procedure for extraction of damping characteristics and modulus of elasticity, Materials Science and Engineering A 370 (2004), 412-416.

[9] S. Patsias, N. Tassini and K. Lambrinou, Ceramic coatings: Effect of deposition method on damping and modulus of elasticity for yttria-stabilized zirconia, Materials Science and Engineering A 442(1-2) (2006), 504-508.

[10] N. A. Cumpsty, Jet Propulsion: A Simple Guide to the Aerodynamics and Thermodynamic Design and Performance of Jet Engines, 2nd Edition, Cambridge University Press, Cambridge, U. K., 2003, Chap 1.

[11] MIL-HDBK-5H, Metallic Materials and Elements for Aerospace Vehicle Structures, AFRL/MLSC, 2179 Twelfth St., Room 122, Wright-Patterson AFB, OH 45433-7718, 1998.

[12] O. T. Easterday, An Experimental Characterization of Damping Properties of Thermal Barrier Coatings at Elevated Temperatures, Ph.D. Dissertation, AFIT/DS/ENY/11-17, Dept. of Aeronautics and Astronautics, Air Force Inst. of Tech., WPAFB, OH, 2011.

[13] A. A. DeLeon, Finite Element Evaluation of an Experiment Related to Coating Damping Properties, M.S. Thesis, AFIT/GA/ENY/09-M03, Graduate School of Engineering and Management, Air Force Institute of Technology (AU), Wright Patterson AFB, OH, 2009.

[14] P. Torvik and B. Runyon, Estimating the loss factors of plates with constrained layer damping treatments, AIAA JOURNAL 45(7) (2007).

[15] N. Tassini, K. Lambrinou, I. Mircea, M. Bartsch, S. Patsias and O. Van der Biest, Study of the amplitude-dependent mechanical behaviour of yttria-stabilised zirconia thermal barrier coatings, Journal of the European Ceramic Society 27 (2006), 1487-1491.

[16] S. Reed, A. Palazotto and W. Baker, An experimental technique for the evaluation of strain dependent material properties of hard coatings, Journal of Shock and Vibration 15(6) (2008), 697-712.

[17] R. Siegel and J. Howell, Thermal Radiation Heat Transfer, Volume 1, 4th Edition, Taylor & Francis, New York, NY, 2002, pp. 598.

[18] A. Campo and R. Villasenor, Subregion of validity of the lumped-based model for transient, radiative cooling of spherical bodies to a zero temperature sink, International Communications in Heat and Mass Transfer 23(6), 855-864.

[19] Abaqus/CAE Users Manual, Dassault Systèmes Simulia Corp., Providence, RI, USA, 2009.

[20] A. Bohnert, Thermal Characterization of a Hall Effect Thruster, M.S. Thesis, Dept. of Aeronautics and Astronautics, Air Force Inst. of Tech., WPAFB, OH, 2008.

[21] K. Hibbert and I. Sorensen, ABAQUS Theory Manual, Volume 6, Version 6, SIMULIA Systems, Providence, RI 02909.

[22] FLIR Systems Inc., FLIR SC660C IR Camera Users Manual, FLIR Systems, Boston, MA, 2010.

[23] F. P. Incropera and D. P. DeWitt, Fundamentals of Heat and Mass Transfer, 4th Edition, Wiley, New York, 1996.

■